

MICROTREMOR MEASUREMENT AT LIQUEFACTION-INDUCED GROUND DEFORMATION AREA

ALFIANSYAH YULIANUR^{1,*}, TAUFIQ SAIDI¹,
BAMBANG SETIAWAN², SUGIANTO SUGIANTO³, MUHAMMAD RUSDI³

¹Department of Civil Engineering, Faculty of Engineering, Universitas Syiah Kuala,
Jl. Tgk. Syech Abdurrauf 7 Darussalam Kota Banda Aceh 23111, Aceh, Indonesia

²Program Study of Geological Engineering, Faculty of Engineering, Universitas Syiah Kuala,
Jl. Tgk. Syech Abdurrauf 7 Darussalam Kota Banda Aceh 23111, Aceh, Indonesia

³Department of Soil Science, Faculty of Agriculture, Universitas Syiah Kuala,
Jl. Tgk. Hasan Krueng Kalee No.3 Darussalam Kota Banda Aceh 23111, Aceh, Indonesia

*Corresponding Author: fian_7anur@unsyiah.ac.id

Abstract

Liquefaction has caused significant structural failures worldwide, including Indonesia since the liquefaction-induced ground displacement has occurred at the Petobo area during the 2018 Palu earthquake. The manifestation of liquefaction on the ground surface is also still under research scrutiny. Liquefiable soils are cohesionless and loose particulate materials, which are very difficult to sample, hence in-situ testing of microtremor measurement is preferred in this study. This study is aimed to investigate the effectiveness of microtremor method for liquefaction assessment and to examine the characteristics of the measured site. To fulfill these aims, a seismometer was deployed to the devastated site of liquefaction-induced ground deformations at the Petobo area. Fourteen ambient noise measurements were collected and analyzed using horizontal to vertical spectral ratio (HVSr) and neighborhood algorithm (NA). The HVSr analysis suggests that the predominant frequency of the study site is between 0.97 Hz to 1.67 Hz. The NA inversion suggests that the critical layer to liquefy is the top 4 to 6 m. A further examination of the results was carried out by comparing the results of this study to other studies. This examination suggests the effectiveness of the applied method of this study for quick disaster response in liquefaction assessment.

Keywords: Assessment, Disaster, Ground deformation, Liquefaction, Microtremor, Site characterization.

1. Introduction

The soil stratum softens as soil liquefaction occurs, allowing large cyclic deformations to arise and accompanying by loss of shear strength, large shear deformations, ground oscillation, or even flow failure [1, 2]. This phenomenon caused devastating effects on structures in many parts of the world [3, 4], including water infrastructures, i.e., dam, canal, tunnel, retaining wall, and waterpipe. Recently this liquefaction phenomenon represents a significant problem for the Indonesian community since the liquefaction-induced ground displacement was recorded by amateur videos during the Palu earthquake. Even though this liquefaction has been observed since year 745 [5], the manifestation of liquefaction on the ground surface is under research scrutiny [6].

Liquefiable soils are cohesionless and loose particulate materials (i.e., silt, sand, and gravel) [2], which are very difficult to sample to provide representative undisturbed specimens for laboratory testing [7]. Therefore, in-situ testing is preferred for liquefaction susceptibility prediction [8] rather than laboratory testing. Moreover, in-situ testing offers a better opportunity to investigate soil structure, dealing with the arrangement of particle groups, including particle sizes, inclusions, and discontinuities [9]. In addition, several soil characteristics are impossible to model in the laboratory, such as the age of the soil profile, the degree of consolidation and cementation, and the strain history, which affects the potential of a soil to liquefy under cyclic loading [7].

Liquefaction assessment based on shear wave velocity (V_s -based correlation) is desirable as the shear wave velocity of the ground surface can be measured with the non-evasive method (i.e., ambient noise analysis). This non-evasive method can provide both a potentially rapid screening method and a method for assessment of coarse to gravelly soils that cannot be reliably penetrated or reliably characterized with small diameter penetrometers (i.e., standard penetration test (SPT) and cone penetration test (CPT) [10]).

Currently, the best V_s -based correlation available is that of Andrus and Stokoe [11]. This V_s -based correlation is also described in the NCEER Workshop summary papers [1]. Although it is undoubtedly the best of its type, this correlation is less well-defined (more approximate) than either SPT- or CPT-based correlations. This V_s -based correlation is not due only to lack of data (though the V_s field case history database is considerably smaller than that available for SPT and CPT correlation development). V_s does not correlate as reliably with liquefaction resistance as does penetration resistance because V_s is a very small-strain measurement and correlates poorly with a very "large-strain" phenomenon (liquefaction). Small amounts of "aging" and cementation of interparticle contacts can cause V_s to increase more rapidly than the corollary increase in liquefaction resistance. V_s -based correlations for resistance to "triggering" of liquefaction are thus best employed either conservatively, or as preliminary screening tools to be supplemented by other methods.

Ambient noise measurement is a promising in-situ testing tool for disaster quick response actions as the method has several advantages, such as being rapid results, easy, non-destructive, low cost, and feasible at any terrain conditions. Currently, applying this tool for liquefaction assessment in affected disaster areas requires further investigations. Therefore, a study of liquefaction-induced ground deformation based on in-situ measurement of the ambient vibration was carried out. Furthermore,

this study is also aimed to investigate the effectiveness of the ambient noise analysis for liquefaction assessment and to examine the sub-surface characteristics of the liquefiable study site. To fulfill the aims, a seismometer was deployed to the devastated site of liquefaction-induced ground deformations at the Petobo area at Palu-Central Sulawesi due to Palu-Donggala 2018 earthquake. The result of this research provides a better understanding of the ambient noise data analysis on liquefaction assessment. In addition, the techniques proposed in this research is to enable engineers to justify necessary actions for liquefaction assessment. Another contribution of this study is the sub-surface liquefaction profiles of the investigated sites. The findings of this study can be utilized for mitigation efforts related to liquefaction hazards at the investigated sites.

The method of this study can be enhanced for further investigation on areas around the water infrastructure, i.e., irrigation canal at Petobo and the surrounding areas. Several researchers reported a significant contribution of the water flow in this irrigation canal to the liquefaction mechanism at the investigated site.

2. Geology Regional at Palu and Surrounding Areas

The geological setting of the study site is generally controlled by the active strike-slip Palu-Koro Fault, with the rate of movement up to 3.4 cm annually [12]. This NNW-SSE oriented fault is splitting the Island of Sulawesi in two. This more than 300 km fault zone is easily distinguished in maps from the Makassar Strait towards the Gulf of Bono. Further North, the fault has opened widely to construct a valley which at around Palu area is up to 10 km wide (Fig. 1). Paleoseismic studies suggested three major earthquakes (>6.8 Mw) occurred along this Palu-Koro Fault in the last 2,000 years, or one such earthquake every 700 years [13]. The recent significant earthquake of magnitude 7.5 on September 28, 2018, has been highlighted by Walpersdorf et al. [14] and Watkinson and Hall [15]. This 2018 earthquake was struck on the Palu-Koro fault, which has a slip rate faster than the San Andreas fault. This Palu-Koro fault straddle by the city of Palu with a population of about 340,000. This seismic event caused 2,045 casualties, 10,679 injuries, 82,775 people reported displaced, and 671 people reported missing. There was amateur video evidence of liquefaction triggered by an earthquake at the Petobo area, Central Sulawesi, Indonesia. The liquefaction at Petobo affected at least 1.8 square kilometers, destroyed up to 744 houses, and caused more than 104 fatalities.

Figure 1 shows the geological map of Palu and the surrounding areas [16]. Generally, the Palu depression area is filled with Quaternary, i.e., Holocene sediments (Fig. 1). In the middle of the Palu Basin were deposited alluvial materials such as clay, silt, and sand. This alluvium constitutes alluvial flood materials and old river channel deposits. These alluvial materials are spatially distributed along with the low level of Palu River near the mid of the valley [13].

Further up reduce level from the center of the valley, there are mixed young and old alluvium fan deposits, which consist of surficial sediments from the low to medium relief hills. These unconsolidated alluvium fans lay along with the tributary drainage systems near the base of the mountains [17]. The site of this study is located at 8.5 km SE of the Palu River mouth (the big black circle in Fig. 1). At the edges of both east and west borders of the Palu, depression was filled by colluvial wedges of gravelly sands at higher elevations [17]. The gravel is schist, igneous, and sedimentary rocks. Generally, the bedrock depth in the Palu depression is estimated

between less than 25 m to greater than 125 m. In the Palu basin, this depth of bedrock, as expected, is increasing towards the center of the valley [18]. This bedrock depth also increases moving relatively north-west and reaches the greatest depth at the Palu River mouth [18]. Generally, the basement rock in this Palu depression consists of metamorphic complexes and Late Pliocene granitoids [19]. The phreatic water table at the study site is estimated between 0.5 m to 4 m below the ground level [20].

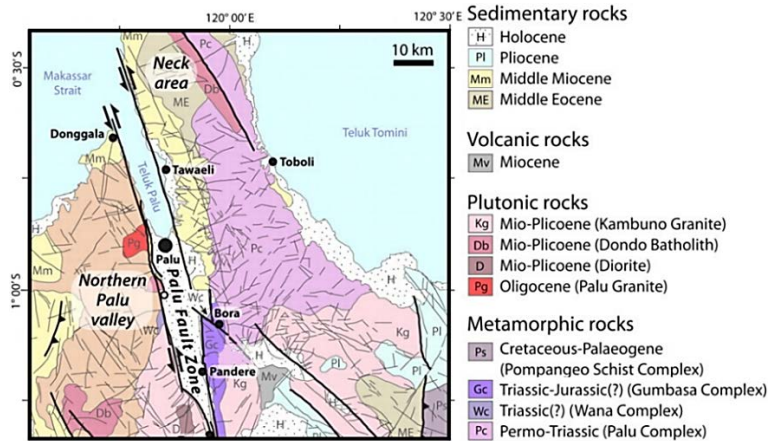


Fig. 1. Geological map of the Palu and the surrounding areas [16].

3. Methodology

A microtremor is one of the most common methods used in urban environments as it is low-cost, efficient, and requires no artificial energy excitation, i.e., hammer, rammer, bomb. This microtremor can be used to deduce several subsurface characteristics, i.e., bedrock depth, site fundamental frequency, and shear wave velocity [21-32]. Single station microtremor data can be processed using a horizontal to vertical spectral ratio (HVSR) method. This HVSR method is an experimental technique. This HVSR method is based on the spectral ratio analysis between the Fourier amplitude spectrum of the horizontal (H) and vertical (V) components of the recorded microtremor [33].

This study focuses on the evaluation of soil liquefaction utilizing microtremor data analysis. Microtremor field measurements were carried out at the devastated site of liquefaction-induced ground deformations at Petobo, Palu-Central Sulawesi, Indonesia. The data were analyzed to deduce some findings of the study. The adopted methodology is outlined in the following sections.

Microtremor measurements at 10 (ten) location inside the affected zone were carried out. Four (4) locations of microtremor measurements outside the liquefaction affected area were also carried out. In addition, soil investigation using a mechanical cone penetration test (m-CPT) by Widyaningrum [20] is shown in the yellow square box to allow some comparisons later. In accordance with [20] study, the site was classified into three different liquefaction zones, which are high potential liquefaction zone, low potential liquefaction zone, and un-classified zone. Figure 2 presents the locations of microtremor measurements at the study area incorporated zoning study by Mason et al. [34] and the nearest m-CPT by Widyaningrum [20].

2.1. Equipment and field setting

The equipment used to acquire the data consists of a seismometer (Fig. 3(a)), a global positioning system (GPS) antenna (Fig. 3(b)), a portable battery (Fig. 3(c)), and a laptop computer. The seismometer used to acquire the microtremor data is a tri-axial sensor of the Guralp CMG 6TD broadband seismometer with a built-in digitizer. A satellite GPS antenna is for the positioning and timing of the recording. A 12V 7A battery was used to power the system. Finally, a portable computer is used for setting the initial setup and checking the recording progress.

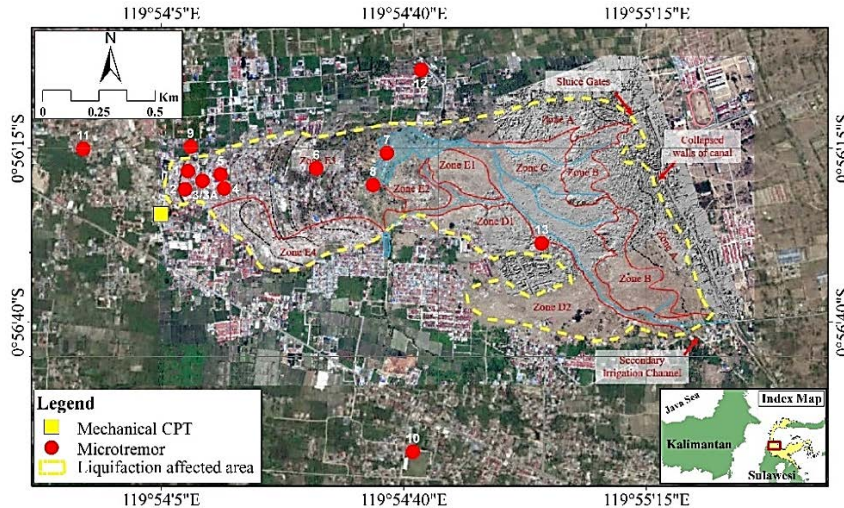


Fig. 2. Locality and locations of microtremor measurements at the Petobo area of Central Sulawesi incorporated zoning study by Mason et al. [34] and the nearest mechanical cone penetration test (m-CPT) by Widyaningrum [20].

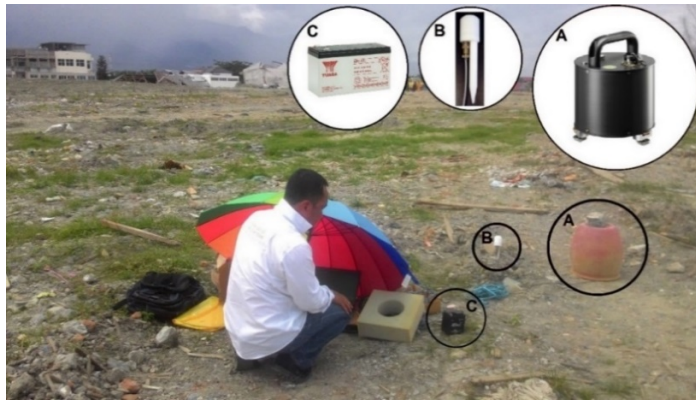


Fig. 3. The used main equipment, i.e. (a) seismometer, (b) GPS antenna, (c) battery and setting of the equipment on site.

In the field measurement, the seismometer was set over the cleared ground surface, as shown in Fig 3. The North oriented seismometer was protected with a plastic bucket and stabilized with a masonry brick to minimize any instability

during recording. The field survey data sheet to record any disturbances during the measurement and field conditions was also prepared and filled.

2.2. Data processing

Initially, a merging of 10-minute noise data to create 30-minute duration waveform datasets was carried out. This minimum 30-minute duration datasets for further analysis is suggested by the Site Effects Assessment using Ambient Excitation (SESAME) [35] and applied by Setiawan et al. [36]. This merging process was carried out for the 3 orthogonal directions of the waveforms (two horizontal and one vertical).

The 30-minute ambient noise datasets were post-processed using Geopsy Software Package [33] to obtain the horizontal to vertical spectral ratio (HVSr) ellipticity curve. This Geopsy software was developed within the SESAME Project framework. Any presence of industrial wave sources in the 30-minute datasets was investigated before the HVSr analysis. This process is to justify the applicability of the dataset used in the HVSr analysis. An ellipticity curve produced by HVSr analysis is used to estimate the predominant frequency of the measured site.

Many studies suggested that the HVSr ellipticity curve can also be used for profiling the shear wave velocity of the measured site [29, 31]. A stratigraphic constraint developed from several previous studies at Petobo and the surrounding areas was incorporated in the inversion process. Detailed stratigraphic parameters for all the measured sites are presented in Table 1, which is developed from previous studies, i.e., [17, 18, 20, 34]. The shear wave velocity inversion was carried out using the Dinver code [37], which was developed using the neighborhood algorithm (NA) of Sambridge [38]. The NA is a stochastic direct-search method to find an acceptable model inside a multidimensional parameter space. Like other direct-search methods, the NA creates pseudo-random samples in the parameter space using the HVSr ellipticity curves constraint provided [37]. In this study, the best 20 shear wave velocity (V_s) profiles were extracted from about 5000 generated models in 2 to 4 trials at each measured site. These 20 shear wave velocities are representing the lowest 20 misfit inversions of the HVSr ellipticity curves. The mean shear wave velocities are subsequently calculated to obtain the ground shear wave velocity model of the measured site.

Table 1. Test model specifications and test conditions.

Layer No.	Depth (m)	Compression wave velocity (m/s)	Poisson's ratio	Shear wave velocity (m/s)	Density (kg/m ³)
Layer#1	1 - 10	1600 - 2000	0.2 - 0.5	100 - 350	1800 - 2000
Layer#2	5 - 20	1600 - 2000	0.2 - 0.5	150 - 500	1800 - 2000
Layer#3	10 - 100	1600 - 2000	0.2 - 0.5	150 - 1000	1800 - 2000
Layer#4 ¹	>100	1600 - 5000	0.2 - 0.5	500 - 3500	1800 - 2000

¹Layer#4 > Layer#3

4. Results

This research focuses on the application of single microtremor measurements at the liquefiable site. Microtremor data at the liquefiable site of the Petobo area at Central Sulawesi of Indonesia were analyzed. The results, including the HVSr curve, site

predominant frequency, and inverted shear wave velocity profile at the measured sites, were presented in the following sections.

4.1. HVSR curves and site predominant frequency

HVSR curves at all measured locations are shown in [39]. Four different curve models are obtained in this study (Fig. 4). The first curve model is generally showing an apparent peak curve for all trials, as shown in Fig. 4(a). An apparent peak curve for all trials is found at Locations #04, #05 and #11. The second curve model is relatively scattered undulating curves that are found at Locations #01, #02, #03, #10, #12, and #13, as shown in Fig. 4(b). The next curve model is a gently bump curve. This model is suggested at Locations #06 and #07 (see Fig. 4(c)). The last HVSR curve model is a relatively flat curve, which is found at Locations #08 and #09. This model is shown in Fig. 4(d). Analysis of HVSR was almost unable to capture an apparent and reliable HVSR peak curve at Location #02.

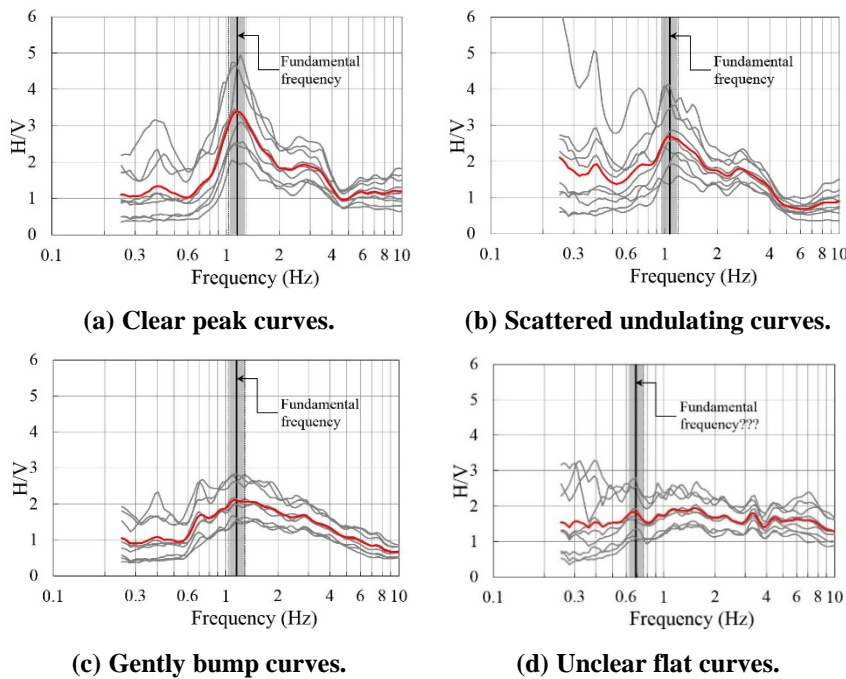


Fig. 4. Four different calculated HVSR curves models are deduced in this study.

To deduce site predominant frequency of f_0 SESAME [35] recommended a process of screening the reliability of the HVSR curve, which is as follows:

- In this study, the peak of the HVSR curve is considered significant if the fundamental frequency, f_0 , is more than 0.4.
- The number of significant cycles must be more than 200.
- The amplitude of the HVSR curve standard deviation, at frequencies from $0.5f_0$ to $2f_0$, must be less than 2 when $f_0 > 0.5$ Hz, or less than 3 when $f_0 < 0.5$ Hz.

Only the f_0 that passes the aforementioned SESAME [35] reliability criteria are used to deduce the site predominant frequency. Generally, the site predominant frequency at most of the sites in the study area is estimated to be around 1 Hz, and only a measured location (#10) is clearly below 1 Hz.

A clear peak predominant frequency is indicated at Locations #01, #02, #03, #04, #07, #08 and #09, whereas Locations #05, #06 and #10 suggested otherwise. The HVSR analysis at Locations #1, #2, and #3 are unable to obtain a distinct and reliable frequency. Furthermore, additional secondary peaks at low amplitudes (i.e., with $H/V \approx 4$) are detected at Locations #01, #02, #03, #08 and #09, as shown in related figures in Appendix A. These secondary peaks are in a frequency between 4 Hz and 6 Hz. These two or three-peaks structure suggests two or three different impedance contrasts at two or three different depth (cf [35, 40]). Since the greatest amplification is at approximately the lowest site predominant frequency, known as the site fundamental frequency [41], thus this lowest frequency is used to justify the frequency of the site. Figure 5 shows the amplitude at f_0 of all the trials at all locations, with failed trials from the SESAME [35] criteria identified in the red-circle, and all passed trials (diamond blue) at all locations. The tabulation of predominant frequency at all measured sites is shown in Table 2 which suggests the site predominant frequency, as follow: 0.97 - 1.03 Hz for Location#01, 1.44 Hz for Location#02, 1.10-1.15 Hz for Location#03A/03, 1.15-1.25 Hz for Location#04, 1.12- .24 Hz for Location#05, 1.22 - 1.49 Hz for Location#06, 1.30 - 1.38 Hz for Location#07, 1.22 - 1.55 Hz for Location#08, 1.47 Hz for Location#09, 1.13-1.20 Hz for Location#10, 1.11-1.15 Hz for Location#11, 1.16-1.25 Hz for Location#12, and 1.44-1.67 Hz for Location#13.

Table 2. Tabulation of estimated site predominant frequency.

Location No.	Estimated Site Predominant Frequency (Hz)			
	Trial#1	Trial#2	Trial#3	Trial#4
#01	0.34*	1.03	0.98*	0.97
#02	1.18*	1.17*	1.24*	1.44
#03A	1.10	1.15	1.14	N/A ¹
#03	2.27*	1.15	1.49*	1.01
#04	1.15	1.21	1.25	N/A ¹
#05	1.24	1.15	1.12	N/A ¹
#06	1.33	1.22	1.49	N/A ¹
#07	1.38	1.34	1.30	N/A ¹
#08	1.22	1.55	0.72*	N/A ¹
#09	1.11*	1.47	N/A ¹	N/A ¹
#10	1.18	1.13	1.20	0.91*
#11	1.15	1.11	1.13	1.13*
#12	1.16	1.24*	1.25	N/A ¹
#13	1.67	2.81*	1.44	3.75*

* fail to comply with SESAME [35] reliability criteria.

¹ N/A is not available.

4.2. Shear wave velocity profile

In this study, the shear wave velocity profile is obtained by inverting the HVSR ellipticity curve, as shown in Appendix B. As aforementioned, in the inversion of the HVSR ellipticity curve 4 main parameters associated with each layer: the compression wave velocity, Poisson's ratio, shear wave velocity, and density were

adopted. In this study, the profile of the measured site is expected to be generally soft at the top layer of between 1 and 10 m depth. It is followed by different characteristic layers from 5 to 20 m depth or 10 to 100 m depth before encountering the hard layer (bedrock) at below 100 m depth. Each layer depth is given in a range to allow the inversion algorithm to explore for the best fit model to the HVSR ellipticity curve provided. More than 5000 models were generated in the inversion, from which 20 best models were extracted and averaged, subsequently. Appendix A presents the mean shear wave velocity profile of all trials in each location. These profiles are compared against the nearest estimated shear wave velocity deduced from the borehole standard penetration test (SPT) in [20]. The estimated shear wave velocity from the SPT is deduced using [42] approach. Most all the measured locations are overestimated the estimated shear wave velocity of the SPT, except for Location #13.

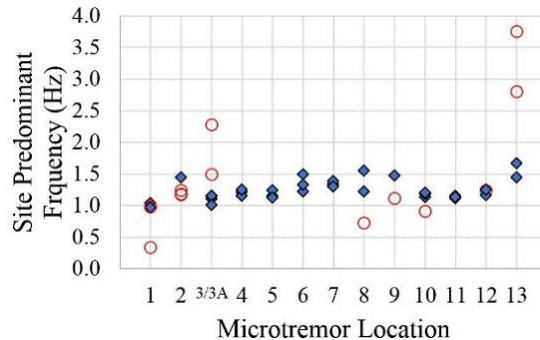


Fig. 5. Estimated site predominant frequency for all trials at all measured locations (red circles are failed trials, and blue diamonds are passed trials of SESAME [35] reliable criteria).

5. Discussion

The estimation of site predominant frequency of this study is in a good agreement to Thien et al. [18]. The site frequency of 1 Hz or above is suggested. A high of site predominant frequency at the liquefaction site was also suggested by Karimzadeh and Matsuoka [43]. Furthermore, the site predominant frequency also can be used to estimate the bedrock depth [21, 32, 43]. Therefore, the results of site predominant frequency of this study suggest a relatively shallow bedrock level at all the measured locations. A raw estimation of the bedrock depth using the generic function of Kramer [41] at the study site could be between 20 to 90 m below the ground level. The bedrock depth estimation also can be estimated using the empirical functions of Seht and Wohlenberg [44] and Parolai et al. [21]. Both the Seht and Wohlenberg [44] and Parolai et al. [21] function could estimate the bedrock depth at the study site of between 50 m and 110 m. Generally, these bedrock depth estimations of this study are in good agreement to the study by Thien et al. [18].

In the case of liquefaction evaluation based on the shear wave velocity threshold (180 m/s), as suggested in Youd et al. [1], there is no liquefaction potential at most of the measured sites. Assuming densification doesn't occur during the liquefaction, the shear wave velocity profiles developed in this study suggest that only the top 6 m at Location #13 layer is vulnerable to liquefy ($V_s < 180$ m/s) at inside liquefaction zone of the study site (Fig. 1). In fact, devastating liquefaction occurred at most of

the measured sites during the Palu Donggala 2018 earthquake. The morphology of the Petobo liquefaction site before the 2018 liquefaction was a gently sloping ground with an estimated slope between 2 % to 8 %, as shown in Fig. 6. The generated digital elevation model before the disaster suggested highly relief from the mid-western part to the end east of the liquefaction affected area boundary. Investigating the groundwater at the Petobo affected liquefaction area, Fig. 7, suggests that the flow direction of the 2018 liquefaction tends to follow the direction of the gradient hydraulic of the groundwater.

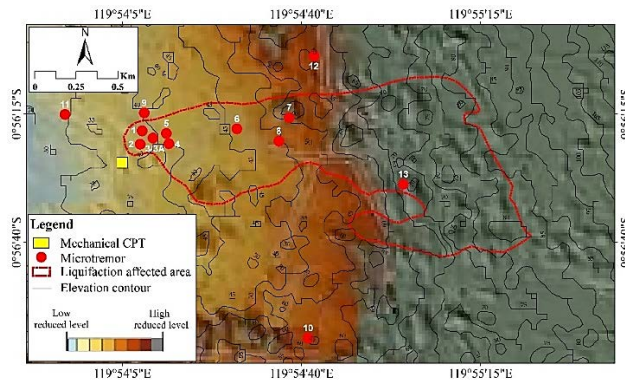


Fig. 6. Generated digital elevation model before the disaster incorporated the location of the microtremor measurement of this study and the location of m-CPT of [20].

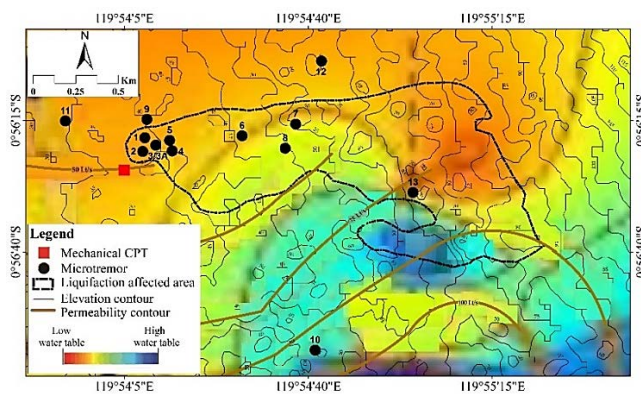


Fig. 7. Overlaying the single microtremor measured location on the phreatic water table and the permeability contour of deep groundwater of [45].

The liquefaction vulnerability of Palu and the surrounding areas has been investigated before the 2018 disaster by Widyaningrum [20]. The affected liquefaction area of Petobo is classified as a highly potential liquefaction zone, as shown in Fig. 8. The figure also presents the locations of the single ambient noise measurement of this study.

Further analysis was carried out using the developed V_s profiles, as shown in Fig. 9. Based on the microtremor data analysis, the developed shear wave velocity

profiles of this study suggest that two measured locations, i.e., #10 and #13, are in a high potential to liquefy (<180 m/s), as presented in Fig. 9(c). This finding is overestimated the results of [20], which suggested the low potential to unidentified (no liquefaction) for locations #10 and #13, respectively. The present study also suggests a medium potential to liquify at five other tested locations, i.e., #01, #03, #03A, #05, and #09, as shown in Fig. 9(b). All these 5 locations are around the toe of the 2018 liquefaction flow, as shown in Figs. 6 to 8. This finding suggests a high liquefaction vulnerability around the toe of the 2018 liquefaction zone provided soil fines content is less than 35 % [1], and groundwater flow is uncontrolled [34].

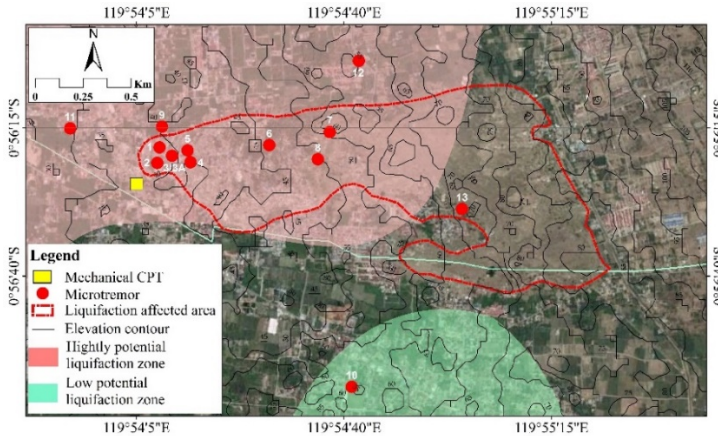


Fig. 8. Developed the liquefaction zone at Petobo and the surrounding areas by Widyaningrum [20] incorporated the location of the microtremor measurement of this study and the location of m-CPT of [20].

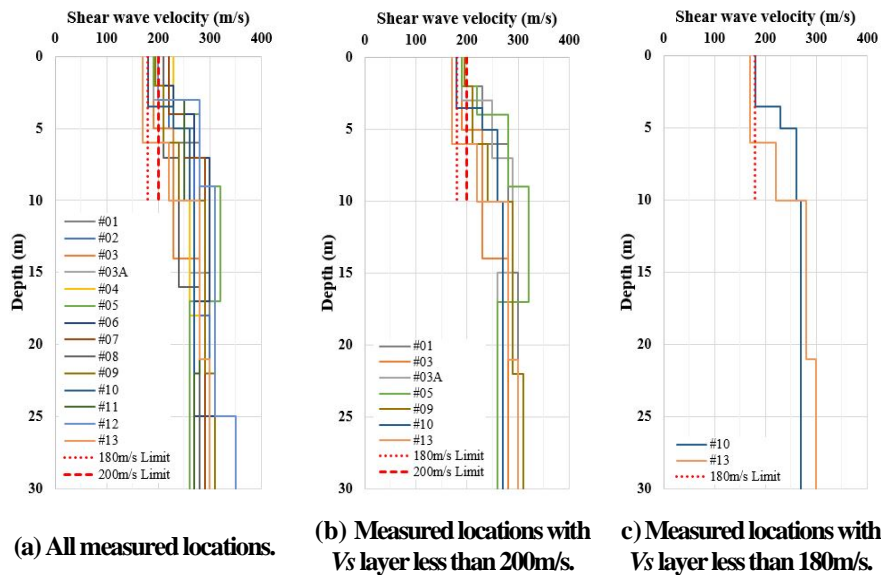


Fig. 9. Shear wave velocity profiles

6. Conclusion

Liquefaction has caused a significant problem for the community. This study seeks to address the characteristics of the liquefaction-induced ground deformation at Petobo and the applicability of single ambient noise data analysis for evaluating soil liquefaction. Fourteen microtremor measurements using Guralp CMG 6TD seismometer were obtained at various locations across the liquefaction area of Petobo. This study presents an analysis of the horizontal to vertical spectral ratio (HVSr) method and the inversion of the HVSr ellipticity using the neighborhood algorithm (NA) to assess the liquefaction of the soil. This study suggests that the predominant frequency of the study site is between 0.97 Hz to 1.67 Hz, and the top 4 to 6 m thick layer at the study site is the critical layer to liquefy. These results are compared with other studies and boreholes drilled near the study site. The results of the analyses suggest that the single ambient noise data method is useful for rapid liquefaction evaluation, including liquefaction assessment for water facilities site. Furthermore, this study also suggests a contribution of the groundwater flow to the liquefaction mechanism at the investigated site.

Nomenclatures

f_0	Site predominant frequency
M_w	Local Magnitude
V_s	Shear wave velocity

Abbreviations

CPT	Cone Penetration Test
GPS	Global Positioning System
HVSr	Horizontal Vertical Spectral Ratio
m-CPT	Mechanical Cone Penetration Test
N/A	Not Available
NA	Neighbourhood Algorithm
NCEER	National Center for Earthquake Engineering Research
NNW	North-North West
SE	South East
SESAME	Site Effects Assessment using Ambient Excitation
SPT	Standard Penetration Test
SSE	South-South East

References

1. Youd, T.L.; Idriss, I.M.; Andrus, R.D.; Arango, I.; Castro, G.; Christian, J.T.; Dorby, R.; Finn, W.D.L.; Harder, J.L.F.; Hynes, M.E.; Ishihara, K.; Koester, J.P.; Liao, S.S.C.; Marcuson III, W.F.; Martin, G.R.; Mitchell, J.K.; Moriwaki, Y.; Power, M.S.; Robertson, P.K.; Seed, R.B.; and Stokoe II, K.H. (2001). Liquefaction resistance of soils: Summary report from the 1996 NCEER and 1998 NCEER/NSF workshops on evaluation of liquefaction resistance of soils. *Journal of Geotechnical and Geoenvironmental Engineering*, 127(10), 297-313.
2. Ahmad, M.; Tang, X.-W.; Ahmad, F.; and Jamal, A. (2018). Assessment of soil liquefaction potential in Kamra, Pakistan. *Sustainability*, 10(11), 4223.

3. Boulanger, R.W.; Munter, S.K.; Krage, C.P.; and DeJong, J.T. (2019). Liquefaction evaluation of interbedded soil deposit: Çark Canal in 1999 M7.5 Kocaeli Earthquake. *Journal of Geotechnical and Geoenvironmental Engineering*, 145(9), 05019007.
4. Sonmez, B.; Ulusay, R.; and Sonmez, H. (2008). A study on the identification of liquefaction-induced failures on ground surface based on the data from the 1999 Kocaeli and Chi-Chi earthquakes. *Engineering Geology*, 97(3), 112-125.
5. Wakamatsu, K. (2000). Liquefaction history, 416-1997, in Japan. *In Proceedings of the 12 World Conference on Earthquake Engineering*, 2270, 8.
6. Bray, J.; and Dashti, S. (2014). Liquefaction-induced building movements. *Bulletin of Earthquake Engineering*, 12, 1129-1156.
7. Glaser, S.D.; and Chung, R.M. (1995). Estimation of Liquefaction Potential by In Situ Methods. *Earthquake Spectra*, 11(3), 431-455.
8. Martin, G.R.; and Lew, M. (1999). *Guidelines for analyzing and mitigating liquefaction hazards in California*. Southern California Earthquake Center: University of Southern California.
9. Johnston, I.W. (1983). *Why ins-situ testing?*. An Extension Course on in-situ testing for Geotechnical investigation.
10. Ghafghazi M.; DeJong J. T.; and Wilson, D. (2017). Evaluation of becker penetration test interpretation methods for liquefaction assessment in gravelly soils. *Canadian Geotechnical Journal*, 54, 1272-1283.
11. Andrus, R.D.; and Stokoe II, K.H. (2000). Liquefaction resistance of soils from shear-wave velocity. *Journal of Geotechnical and Geoenvironmental Engineering*, 126 (11), 1015-1025.
12. Socquet, A.; Simons, W.; Vigny, C.; McCaffrey, R.; Subarya, C.; Sarsito, D.; Ambrosius, B.; and Spakman, W. (2006). Microblock rotations and fault coupling in SE Asia triple junction (Sulawesi, Indonesia) from GPS and earthquake slip vector data. *Journal of Geophysical Research: Solid Earth*, 111(B8), 1-15.
13. Bellier, O.; Sébrier, M.; Seward, D.; Beaudouin, T.; Villeneuve, M.; and Putranto, E. (2006). Fission track and fault kinematics analyses for new insight into the Late Cenozoic tectonic regime changes in West-Central Sulawesi (Indonesia). *Tectonophysics*, 413(3), 201-220.
14. Walpersdorf, A.; Vigny, C.; Subarya, C.; and Manurung, P. (1998). Monitoring of the Palu-Koro fault (Sulawesi) by GPS. *Geophysical Research Letters*, 25(13), 2313-2316.
15. Watkinson, I.M.; and Hall, R. (2016). Fault systems of the eastern Indonesian triple junction: evaluation of quaternary activity and implications for seismic hazards. *Geological Society, London, Special Publications*, 441, 71-120.
16. Watkinson, I.M. (2011). Ductile flow in the metamorphic rocks of central Sulawesi. *Geological Society, London, Special Publications*, 355(1), 157-176.
17. Sukanto, R.; Sumadirdja, H.; Suptandar, T.; Hardjoprawiro, S.; and Sudana, D. (1994). *Peta Geologi Lembar Palu, Sulawesi, Indonesia Skala 1:250.000*. "Regional geological map of Palu sheet, Indonesia, scale 1:250,000". Bandung, Indonesia: Geological Research Center.
18. Thein, P.S.; Pramumijoyo, S.; Wilopo, W.; Setianto, A.; Brotopuspito, K.S.; and Kiyono, J. (2014). Estimation of subsurface structure based on microtremor, bore hole

- observations and stochastic strong ground motion simulations in Palu City, Central Sulawesi, Indonesia: a validation and sensitivity study on the 23 January 2005 (PALU) earthquake. *Journal of Southeast Asian Applied Geology*, 6(2), 96-108.
19. Sopaheluwakan, J.; Kadarusman, A.; Priadi, B.; and Utoyo, H. (1995). The nature of basement rocks in Palu region, Central Sulawesi. The Newly found eclogite and its regional implication. *Proceedings of Sixth International Congress on Pacific Neogene Stratigraphy and IGCP, 355, 73-39.*, Puspitek Serpong, West Java, Indonesia.
 20. Widyaningrum, R. (2012). *Penyelidikan geologi teknik potensi likuifaksi daerah Palu, Provinsi Sulawesi Tengah. "Geological engineering investigation of liquefaction potential at Palu area, Central Sulawesi"*. Bandung: Kementerian Energi dan Sumber Daya Mineral.
 21. Parolai, S.; Bormann, P.; and Milkereit, C. (2002). New relationships between Vs, thickness of sediments, and resonance frequency calculated by the H/V ratio of seismic noise for the cologne area (Germany). *Bulletin of the Seismological Society of America*, 92(6), 2521-2527.
 22. D'Amico, V.; Picozzi, M.; Albarello, D.; Naso, G.; and Tropenscovino, S. (2004). Quick estimates of soft sediment thicknesses from ambient noise horizontal to vertical spectral ratios: a case study in southern Italy. *Journal of Earthquake Engineering*, 8(6), 895-908.
 23. Hinzen, K.; Weber, B.; and Scherbaum, F. (2004). On the resolution of H/V measurements to determine sediment thickness, a case study across a normal fault in the Lower Rhine Embayment. *Journal of Earthquake Engineering*, 8(6), 909-926.
 24. Gosar, A. (2007). Microtremor HVSR study for assessing site effects in the Bovec basin (NW Slovenia) related to 1998 Mw5.6 and 2004 Mw5.2 earthquakes. *Engineering Geology*, 91, 178-193.
 25. Dinesh, B.; Nair, G.; Prasad, A.; Nakkeeran, P.; and Radhakrishna, M. (2010). Estimation of sedimentary layers shear wave velocity using micro-tremor H/V ratio measurements for Bangalore city. *Soil Dynamic and Earthquake Engineering*, 30, 1377-1382.
 26. Paudyal, Y.; Yatabe, R.; Bhandary, N.; and Dahal, R. (2012). A study of local amplification effect of soil layers on ground motion in the Katmandu Valley using microtremor analysis. *Earthquake Engineering and Engineering Vibration*, 11(2), 257-268.
 27. Del Gaudio, V.; Muscillo, S.; and Wasowski, J. (2014). What we can learn about slope response to earthquakes from ambient noise analysis: An overview. *Engineering Geology*, 182, 182-200.
 28. Guo, A.; Aydin, A.; and Kuszmaul, J. (2014). Microtremor recordings in Northern Mississippi. *Engineering Geology*, 179, 146-157.
 29. Di Stefano, P.; Luzio, D.; Renda, P.; Martorana, R.; Capizzi, P.; D'Alessandro, A.; Messina, N.; Napoli, G.; Todaro, S.; and Zarcone, G. (2014). Integration of HVSR measures and stratigraphic constraints for seismic microzonation studies: the case of Oliveri (ME). *Natural Hazards and Earth System Sciences Discussion*, 2(4), 2597-2637.
 30. Guo, Z.; and Aydin, A. (2016). A modified HVSR method to evaluate site effect in Northern Mississippi considering ocean wave climate. *Engineering Geology*, 200, 104-113.

31. Setiawan, B.; Jaksa, M.; Griffith, M.; and Love, D. (2018). Seismic site classification based on constrained modeling of measured HVSR curve in regolith sites. *Soil Dynamics and Earthquake Engineering*, 110, 244-261.
32. Setiawan, B.; Jaksa, M.; Griffith, M.; and Love, D. (2018). Estimating bedrock depth in the case of regolith sites using ambient noise analysis. *Engineering Geology*, 243, 145-159.
33. Geopsy (2019). Geopsy home: software applications for ambient vibration. Retrieved July 1, 2019, from <http://www.geopsy.org/>.
34. Mason, H.B.; Gallant, A.P.; Hutabarat, D.; Montgomery, J.; Reed, A.N.; Wartman, J.; Irsyam, M.; Prakoso, W.; Djarwadi, D.; Harnanto, D.; Alatas, I.; Rahardjo, P.; Simatupang, P.; Kawanda, A.; and Hanifa, R. (2019). *Geotechnical Reconnaissance: The 28 September 2018 M7.5 Palu-Donggala, Indonesia Earthquake* (Version 1.0). Indonesia: Report of Geotechnical Extreme Events Reconnaissance.
35. SESAME (2004). *Guidelines for the implementation of the H/V spectral ratio technique on ambient vibrations Measurements, processing, and interpretation*. SESAME European Research Project Wp12.
36. Setiawan, B.; Jaksa, M.; Griffith, M.; and Love, D. (2018). Passive noise datasets at regolith sites. *Data in Brief*, 20, 735-747.
37. Wathelet, M.; Jongmans, D.; and Ohrnberger, M. (2005). Direct Inversion of Spatial Autocorrelation Curves with the Neighborhood Algorithm. *Bulletin of the Seismological Society of America*, 95(5), 1787-1800.
38. Sambridge, M. (1999). Geophysical inversion with a neighbourhood algorithm I. Searching a parameter space. *Geophysical Journal International*, 138, 479-494.
39. Yulianur, A.; Saidi, T.; Setiawan, B.; Sugianto, S.; Rusdi, M.; and Affan, M. (2020). Microtremor datasets at liquefaction site of Petobo, Central Sulawesi-Indonesia. *Data in Brief*, 30, 105554.
40. Guéguen, P.; Chatelain, J.-L.; Guillier, B.; Yepes, H.; and Egred, J. (1998). Site effect and damage distribution in Pujili (Ecuador) after the 28 March 1996 earthquake. *Soil Dynamics and Earthquake Engineering*, 17(5), 329-334.
41. Kramer, S.L. (1996). *Geotechnical Earthquake Engineering*. New Jersey: Prentice Hall
42. Tsiambaos, G.; and Sabatakakis, N. (2011). Empirical estimation of shear wave velocity from in situ tests on soil formations in Greece. *Bulletin of Engineering Geology and the Environment*, 70(2), 291-297.
43. Karimzadeh, S.; and Matsuoka, M. (2018). A weighted overlay method for liquefaction-related urban damage detection: A case study of the 6 September 2018 Hokkaido Eastern Iwate earthquake, Japan. *Geosciences*, 8(12), 487.
44. Seht, M.I-V; and Wohlenberg, J. (1999). Microtremor measurements used to map thickness of soft sediments. *Bulletin of the Seismological Society of America*, 89(1), 250-259.
45. Zeffitni, Z. (2013). Potensi airtanah di Cekungan Airtanah (CAT) Palu berdasarkan satuan hidromorfologi dan hidrogeologi. "Groundwater potential in Palu groundwater basin (CAT) based on hydro-morphology and hydrogeology units." *Jurnal Geografi*, 11 (22), 97-106.

Appendix A

Developed Shear Wave Velocity Profiles

In the present work fourteen developed shear wave velocity profiles are shown in Figs. A-1 to A-14. These figures are used to deduce the critical layer at the measured location.

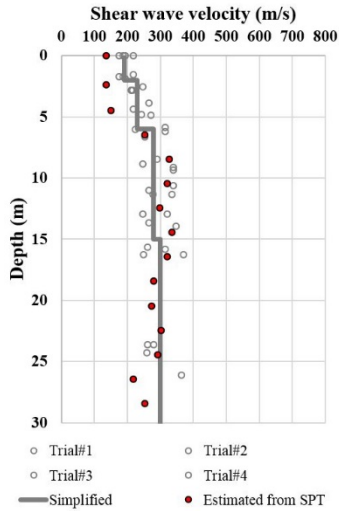


Fig. A-1. Developed shear wave velocity profile constrained by the HVSR ellipticity curve at Location #01.

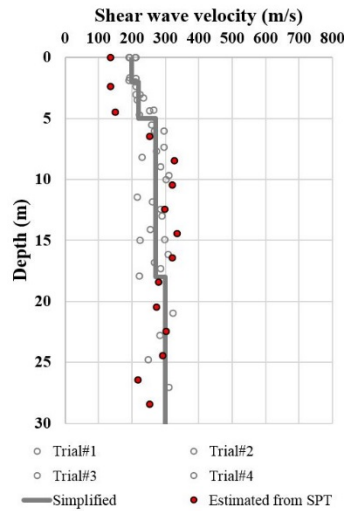


Fig. A-2. Developed shear wave velocity profile constrained by the HVSR ellipticity curve at Location #02.

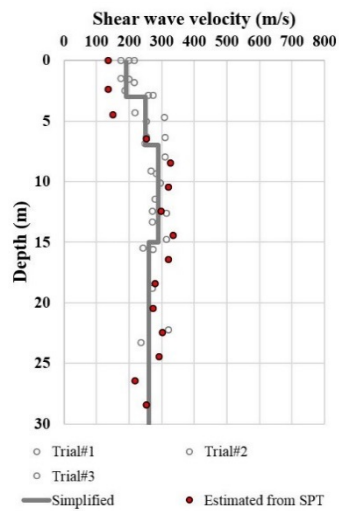


Fig. A-3. Developed shear wave velocity profile constrained by the HVSR ellipticity curve at Location #03A.

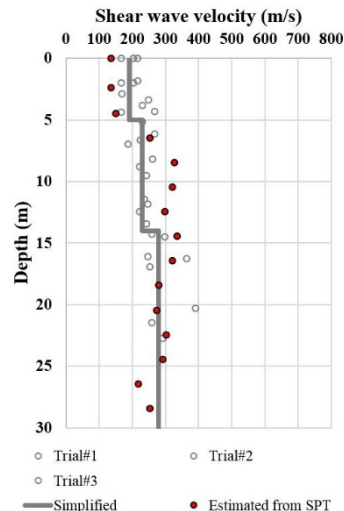


Fig. A-4. Developed shear wave velocity profile constrained by the HVSR ellipticity curve at Location #03.

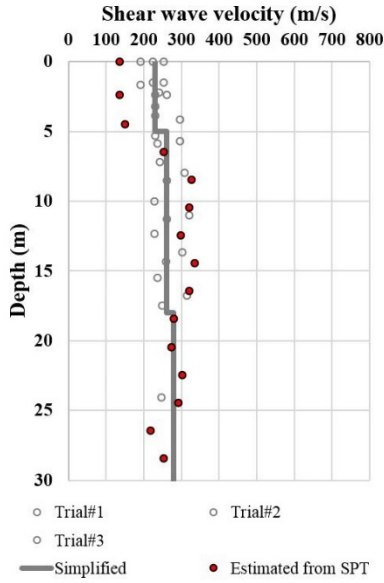


Fig. A-5. Developed shear wave velocity profile constrained by the HVSR ellipticity curve at Location #04.

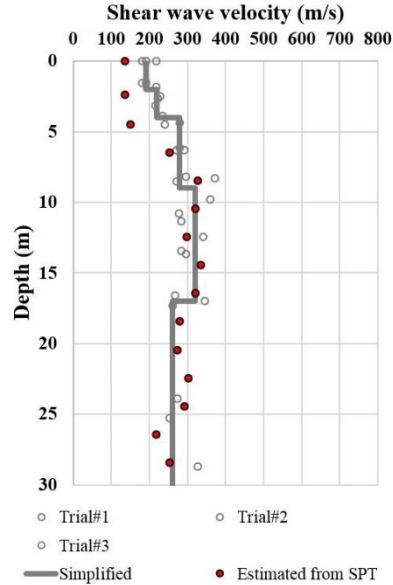


Fig. A-6. Developed shear wave velocity profile constrained by the HVSR ellipticity curve at Location #05.

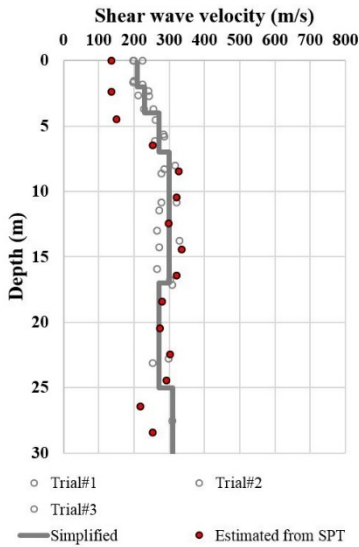


Fig. A-7. Developed shear wave velocity profile constrained by the HVSR ellipticity curve at Location #06.

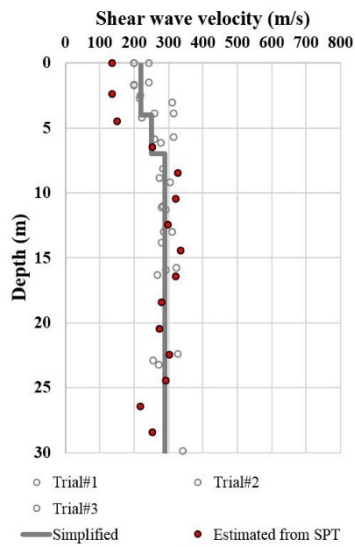


Fig. A-8. Developed shear wave velocity profile constrained by the HVSR ellipticity curve at Location #07.

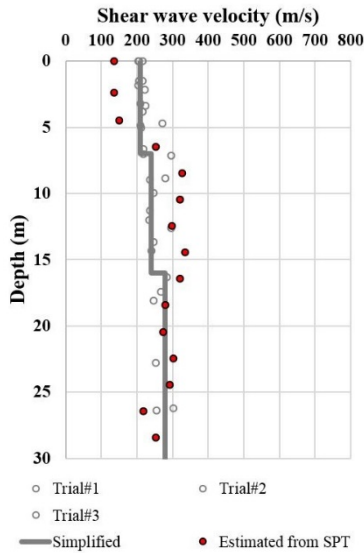


Fig. A-9. Developed shear wave velocity profile constrained by the HVSR ellipticity curve at Location #08.

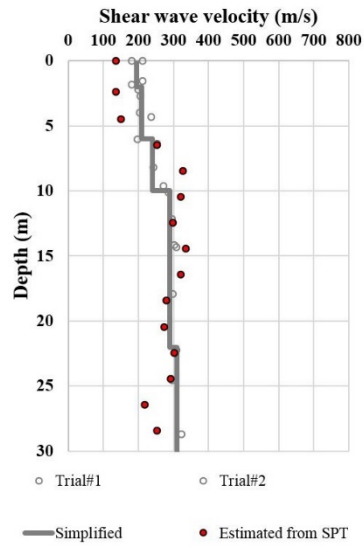


Fig. A-10. Developed shear wave velocity profile constrained by the HVSR ellipticity curve at Location #09.

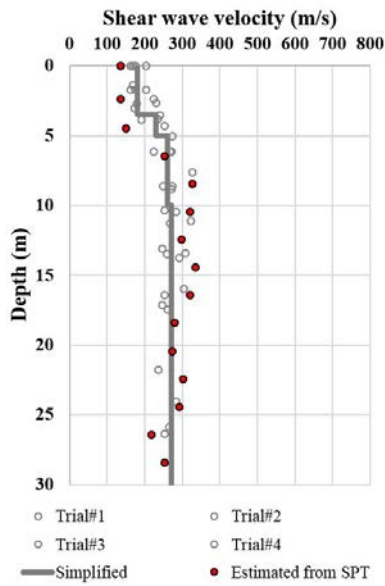


Fig. A-11. Developed shear wave velocity profile constrained by the HVSR ellipticity curve at Location #10.

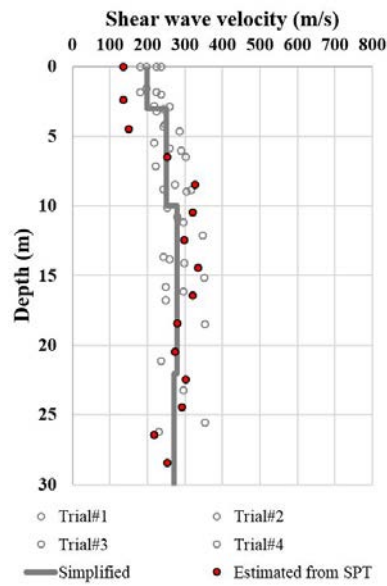


Fig. A-12. Developed shear wave velocity profile constrained by the HVSR ellipticity curve at Location #11.

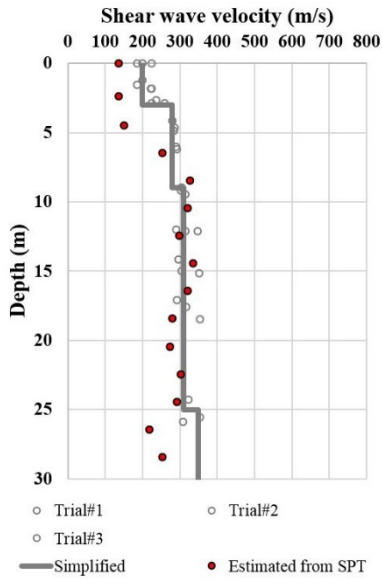


Fig. A-13. Developed shear wave velocity profile constrained by the HVSR ellipticity curve at Location #12.

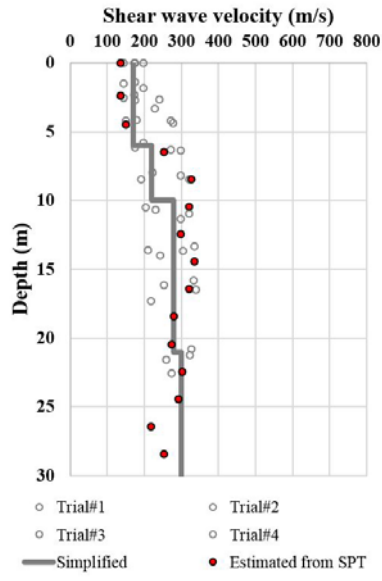


Fig. A-14. Developed shear wave velocity profile constrained by the HVSR ellipticity curve at Location #13.